ACS OMEGA

Open Access

http://pubs.acs.org/journal/acsodf

Article

Novel Magnetic $MnFe_2O_4$-Decorated Graphite-Like Porous Biochar as a Heterogeneous Catalyst for Activation of Peroxydisulfate Toward Degradation of Rhodamine B

Published as part of ACS Omega virtual special issue "Magnetic Nanohybrids for Environmental Applications".

Xinde Jiang,* Zhuoru Tan, Guixian Jiang, Chang Liu, Guiqing Gao, and Zhanmeng Liu*

Cite This: *ACS Omega* 2024, 9, 6455−6465

Read Online

ACCESS | Metrics & More | Article Recommendations

ABSTRACT: A magnetic $MnFe_2O_4$-modified graphite-like porous biochar composite ($MnFe_2O_4$/KFS800) was synthesized by the hydrothermal method, and its catalytic activity was evaluated in the activation of peroxydisulfate toward degradation of Rhodamine B. After characterization by SEM, XRD, and the BET method, the specific surface area and total pore volume of the $MnFe_2O_4$/KFS800 catalyst reached 121 m^2/g and 0.263 m^3/g, and exhibited plate-like morphology with good crystallinity. The degradation rate of Rhodamine B by the obtained composite was more than 91.1% when the initial concentration of RhB was 10 mg/L, the dosage of $MnFe_2O_4$/KFS800 was 0.2 g/L, and the initial pH was 6.7. Then the anti-interference ability of the obtained composite was studied, and it was found that there was a little effect on the degradation of Rhodamine B with the presence of humic acid. Finally, quenching test, EPR research, and XPS analysis were conducted to reveal the catalytic mechanism, and possible mechanism was a synergistic behavior of free radicals ($SO_4^{\bullet-}$, •OH, $O_2^{\bullet-}$) and nonfree radicals ($^1O_2$), and trace amounts of uncarbonized bagasse was also involved in the formation of free radicals.

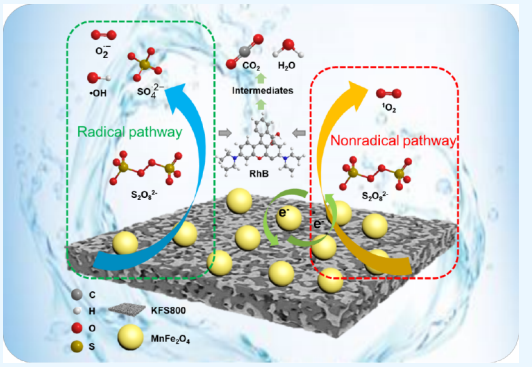

1. INTRODUCTION

With the rapid development of textile industry, a large amount of organic dyes are discharged into natural water environment, resulting in possible threats to the water safety and health of food chain.[1] Therefore, it is necessary to explore efficient technologies for the removal of organic dyes from the wastewater.[2−4] Advanced oxidation processes based on peroxydisulfate (PDS) have attracted increasing attention for the treatment of aqueous contaminants in recent years. Compared to other radicals (•OH), $SO_4^{\bullet-}$ radical shows a lot of advantages during the oxidation process, such as high oxidative capacity, high stability, and long half-life.[5−8] Usually, these excellent radicals are generated by activating PDS via heating,[9,10] light irradiation,[11] acoustic cavitation,[12] carbon materials,[13] and transition metals catalyst.[14] Among these activation methods, transition metal catalysts, such as Co, Mn, Fe, Cu, and Ni, are widely studied because of their high activation efficiency, comparatively low toxicity, and abundant in nature.[15−18]

Heterogeneous activation of PDS by transition metal catalysts has aroused extensive attention for the treatment of organic pollutants.[19] Especially, $MnFe_2O_4$ can be easily separated from the reaction mixture with an external magnetic field after application because of its strong magnetism.[20,21] The size and morphology of $MnFe_2O_4$ could be regulated by varying the reaction condition.[22] Chen et al.[23] have prepared a magnetic $MnO_2/MnFe_2O_4$ nanocomposite by the hydrothermal method, and the decomposition efficiency of this nanocomposite was 90% for RhB within 5 min in the presence of PMS, and radical scavenging experiments have proved that $SO_4^{\bullet-}$ was the primary radical. However, these $MnFe_2O_4$-derived nanocomposites are easy to aggregate in water, resulting in decreased activity sites, restricted mass transfer, and loss of catalytic activity.[24]

The performance of $MnFe_2O_4$ can be enhanced when it is supported with carbonaceous materials, such as graphene,[25] carbon nanotube,[26,27] activated carbon,[28] carbon nanofiber,[29] due to their tunable physicochemical properties and environmentally benign nature. A $MnFe_2O_4$@C-NH_2 catalyst was fabricated that presented high catalytic activity in the antibiotics removal, and the enhanced catalytic activity of

Received: August 23, 2023
Revised: January 18, 2024
Accepted: January 23, 2024
Published: February 2, 2024

materials was ascribed to the carbon shell, which could reduce the aggregation of magnetic nanoparticles and prevented the leaching of metals.[30] The synergistic effect of carbon and $MnFe_2O_4$ catalyst can accelerate the charge transfer at the interfaces, which could impressively boost the catalytic performances.[31,32] However, the catalytic activity could be further improved when $MnFe_2O_4$ was supported with fibrous biochar.[33,34]

In this study, a novel $MnFe_2O_4$/KFS800 catalyst was developed by loading $MnFe_2O_4$ onto graphite-like porous biochar, which was derived from the pyrolysis of fibrous bagasse. The physical and chemical properties of $MnFe_2O_4$ and $MnFe_2O_4$/KFS800 were characterized by scanning electron microscopy (SEM), X-ray diffraction (XRD), vibrating sample magnetometer (VSM), Fourier transform infrared (FTIR), electron paramagnetic resonance (EPR), and X-ray photoelectron spectroscopy (XPS). Batch experiments were performed to investigate the impact of crucial environmental factors on degradation of Rhodamine B (RhB), and recycling tests were conducted to assess the reusability and stability of the catalysts. Combined with these characterizations and identification of the radical species, the synergic effects of $MnFe_2O_4$ and KFS800 toward PDS activation were revealed.

2. MATERIALS AND METHODS

2.1. Materials. $FeCl_3·6H_2O$, $MnCl_2·4H_2O$, $NaHCO_3$, NaCl, NaH_2PO_4, $NaNO_3$, ethanol (EtOH), sodium acetate trihydrate, and ethylene glycol were purchased from Shanghai Aladdin Biochemical Technology Co., Ltd. (China). RhB, *tert*-butyl alcohol (TBA), humic acid (HA), 5, 5-dimethyl-1-pyrroline N-oxide (DMPO), and P-benzoquinone (BQ) were purchased from Shanghai Macklin Biochemical Co., Ltd. (China). Polyethylene Glycol 4000 (PEG 4000) and sodium peroxydisulfate ($Na_2S_2O_8$, PDS) were purchased from Tianjin Kermel Chemical Reagent Co. Ltd. (China). All the chemical reagents used in this study were analytically pure without further purification. The bagasse was obtained from a local institute of sugar cane sugar.

2.2. Preparation of Magnetic $MnFe_2O_4$/KFS800. Synthesis of KFS800: The pyrolysis of clean bagasse was conducted in a tubular furnace at 400 °C for 2 h with a heating rate of 5 °C/min in N_2 atmosphere (100 mL/min). Then, 1 g of bagasse charcoal powder was soaked in 0.1 mol/L (100 mL) potassium ferrate solution, the suspension was mixed by stirring for 8 h, and the residual solids was washed with deionized water, dried in oven at 100 °C for 12 h. Later, the obtained biochar was carbonized in a tubular furnace at 800 °C for 2 h with a heating rate of 5 °C/min in N_2 atmosphere. Finally, the residual solids was washed with ethanol and deionized water five times, respectively, and dried in vacuum at 60 °C for 24 h. The final solids were notated as KFS800 (less than 100 mesh).

Synthesis of $MnFe_2O_4$/KFS800:50 mg of KFS800 was dispersed homogeneously in 40 mL of ethylene glycol under ultrasound for 3 h, and 0.5 mmol of $MnCl_2·4H_2O$ and 1 mmol of Fe $(NO)_3·9H_2O$ were added and mixed by magnetic stirring for 30 min. Then, 0.025 mol sodium acetate trihydrate and 1 g PEG 4000 were added and stirred for another 30 min. After that, the mixed solution was transferred to a Teflon-lined stainless steel autoclave and heated for 12 h at 200 °C. Finally, the obtained product was cooled down to room temperature and centrifuged; the precipitate was washed with ethanol and deionized water five times, and dried in a vacuum oven at 60 °C for 6 h. For comparison, the preparation of pure $MnFe_2O_4$ was synthesized by the same method without adding KFS800.

2.3. Characterization of Magnetic $MnFe_2O_4$/KFS800. The morphology and structure of the $MnFe_2O_4$/KFS800 was observed through a scanning electron microscope (SU8010, Hitachi, Japan) equipped with an EDS analyzer. The magnetic properties of $MnFe_2O_4$/KFS800 were measured by a vibratory probe sample magnetometer (PPMS-9T, Quantum Design Company, USA) at room temperature. The XRD patterns of pristine $MnFe_2O_4$ and $MnFe_2O_4$/KFS800 were investigated by an X-ray diffractometer on a MiniFlex 600 (Rigaku, Japan) with Cu Kα radiation (λ = 1.5406 Å). The surface properties of the samples were analyzed by FTIR spectroscopy (Nicolet 6700, USA) with the KBr method. The specific surface area and pore size of the samples were determined according to nitrogen absorption−desorption isotherm using a volumetric absorption analyzer (Micromeritics ASAP 2460, USA). XPS (Escalab 250Xi, Thermo Fisher Co., UK) was employed to analyze the valence states of the elements on the catalyst surface, and the acquired spectra were calibrated with the C 1s peak at 284.80 eV. To detect the radicals generated in the catalytic reaction, the electron paramagnetic resonance (EPR) tests were conducted on a Bruker A300 spectrometer (Germany) using DMPO as the spin-trapping agent.

2.4. Degradation Experiments. The performance of the $MnFe_2O_4$/KFS800/PDS system was evaluated via a batch of experiments in a 250 mL conical flask at 30 °C containing 100 mL of RhB solution with an initial concentration of 10 mg/L. Typically, the reaction solution was formed by mixing of 50 mL RhB solution (20 mg/L), 20 mL PDS solution (10 mM), and 30 mL deionized water. 1 mol/L H_2SO_4 and NaOH solutions were used to adjust the initial pH, and the pH was measured by a pH meter (model SJ-3F). The reaction was maintained by mechanical stirring, and 2 mL of samples were collected at regular intervals. Then these solutions were quenched with 2.0 mL of methanol and filtered by 0.22 μm membrane, and the absorbance of the filtrate was measured by a UV−vis spectrophotometer (UV-9100, Shanghai) at 554 nm, and all samples were measured in triplicate. The EtOH, TBA, L-his, and BQ were used as quenchers to identify the radical species formed in the catalytic reaction. The degradation experiments were also performed in various catalytic systems, such as PDS (2.0 mM) alone, $MnFe_2O_4$/KFS800 (20 mg) alone, $MnFe_2O_4$/PDS (20 mg/2.0 mM), and $MnFe_2O_4$/KFS800/PDS (20 mg/2.0 mM). The consumption of PDS was determined by iodometric spectrophotometry,[35] 10.0 μL filtrate was mixed with 10.0 mL KI solution (2.0 M), and the reaction was maintained for 10 min by stirring, and the generated I_3^- was measured by the UV−vis method (300−700 nm), and the concentration of I_3^- was proportional to PDS. For the cycling tests, the magnetic separated catalysts were washed with ethanol and water for three times, and redispersed in a fresh RhB solution. The good linearity between $\ln(C_0/C)$ and time suggests that the data are well fitted by the pseudo-first-order kinetic model (eq 1):[36]

$$\ln(C_0/C) = kt \quad (1)$$

where C_0 (mg/L) and C (mg/L) are the RhB concentrations at reaction times of 0 and t, and k (min^{-1}) represents the kinetic constant of pseudo-first-order reaction.

https://doi.org/10.1021/acsomega.3c06278
ACS Omega 2024, 9, 6455−6465

3. RESULTS AND DISCUSSION

3.1. Characterization of $MnFe_2O_4$/KFS800. Figure 1a,b shows the representative SEM images with 50 000 magnification of pristine KFS800 and $MnFe_2O_4$/KFS800, respectively. It could be observed that the original KFS800 exhibited a plate-like morphology and a relatively smooth surface. But the surface of $MnFe_2O_4$/KFS800 became rough, and some solid particles were clearly scattered on the $MnFe_2O_4$/KFS800 surface, which illustrated that $MnFe_2O_4$ particles were loaded onto the KFS800 surface. The EDS (Figure 1c) measurement confirmed the composition of $MnFe_2O_4$/KFS800, which demonstrated the presence of Mn, Fe, C, and O. C mainly comes from the basal plane of KFS800 nanosheets, while O is attributed to both $MnFe_2O_4$ and the residual oxygen-containing functional groups of graphite-like porous biochar.

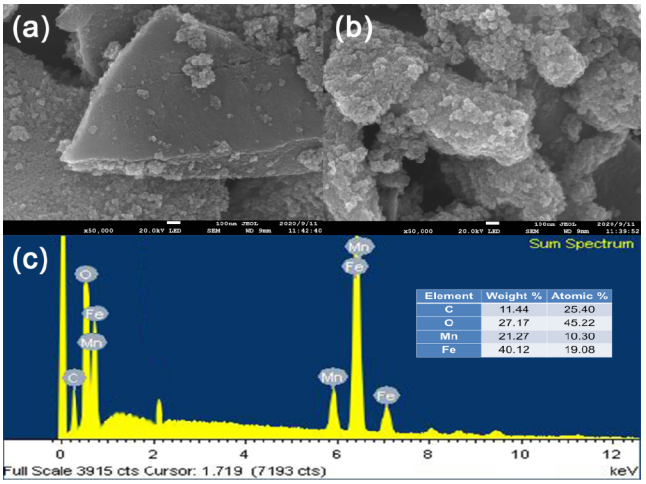

Figure 1. (a) SEM images of KFS800, (b) SEM, and (c) EDS of magnetic $MnFe_2O_4$/KFS800.

The magnetic properties of the pristine $MnFe_2O_4$ and $MnFe_2O_4$/KFS800 were investigated by the VSM technique. As can be seen in Figure 2a, the magnetization curves exhibited a typical S-shape over the applied magnetic field, implying that they are ferromagnetic materials.[37] The saturation magnetization value of $MnFe_2O_4$ and $MnFe_2O_4$/KFS800 was 53.33 and 41.88 emu/g, respectively, and a reasonable explanation for this decrease is the introduction of nonmagnetic KFS800 materials, where this decrease has little effect on recycling of these catalysts by an external magnet (Figure 2a inset).

The crystal phases of magnetic $MnFe_2O_4$ and $MnFe_2O_4$/KFS800 are distinguished by XRD (Figure 2b). The magnetic $MnFe_2O_4$ showed emergence of seven well-defined peaks at 2θ = 18.39°, 30.09°, 35.44°, 43.20°, 53.54°, 56.95°, and 62.57°, which could be attributed to the (111), (220), (311), (400), (422), (511), and (440) crystal planes of spinel-type $MnFe_2O_4$ (JCPDS 10−0319).[38] According to Scherrer's equation, the average size of spinel-type $MnFe_2O_4$ is around 12.4 nm. Besides these seven well-defined peaks, a new peak at 2θ = 23.94° emerged in the $MnFe_2O_4$/KFS800 spectra, which could be attributed to the (002) crystal plane of graphite-like KFS800.

FTIR spectra of the $MnFe_2O_4$/KFS800 composite are shown in Figure 2c, and characteristic vibration bands appeared at 427, 574, 803, 1088, 1259, 1626, 2919, and

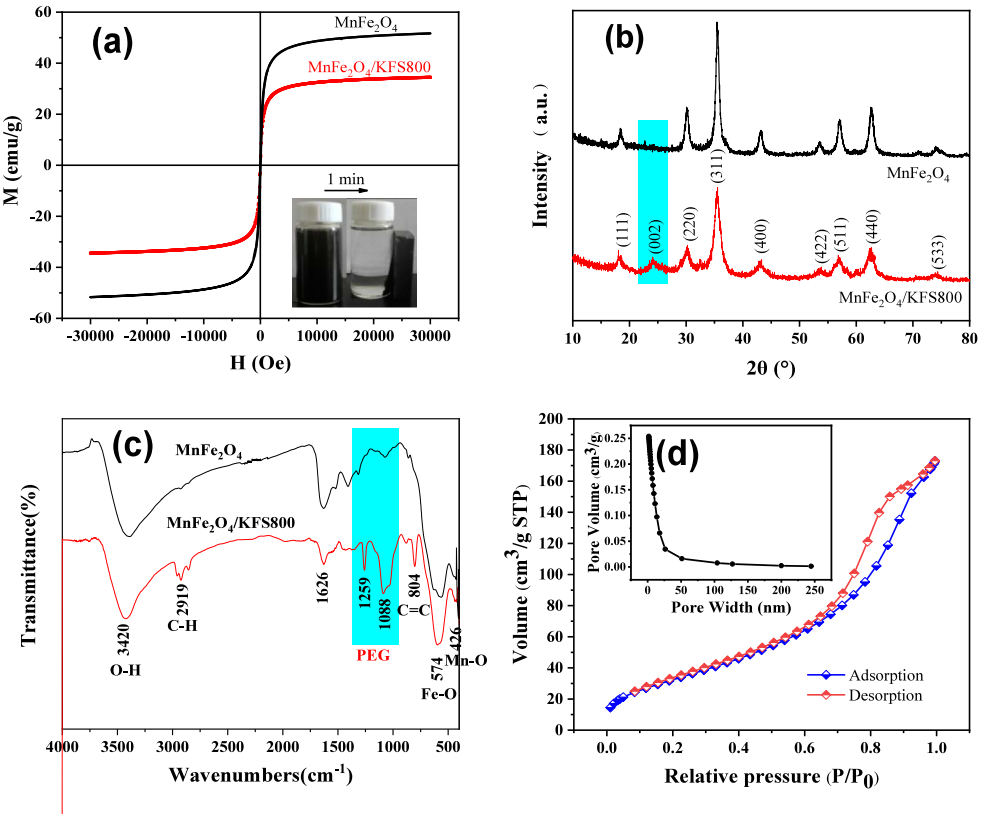

Figure 2. (a) Hysteresis loop, (b) XRD patterns, and (c) FTIR spectra of the $MnFe_2O_4$ and $MnFe_2O_4$/KFS800; (d) N_2 adsorption−desorption isotherms and pore size distribution curves (inset) of the $MnFe_2O_4$/KFS800.

https://doi.org/10.1021/acsomega.3c06278
ACS Omega 2024, 9, 6455−6465

3420 cm^{-1}, respectively. The peak at 3420 cm^{-1} could be attributed to the O−H stretching vibrations of adsorbed water molecules on the nanoparticle surface. The bands at 1259 and 1088 cm^{-1} correspond to the bend style of residual PEG molecules. The observed bands at 574 and 427 cm^{-1} can be attributed to the Fe−O and Mn−O stretching vibration, respectively. Compared to the $MnFe_2O_4$ composite, there are two different characteristic bands appearing at 2919 and 804 cm^{-1} in the spectra of the $MnFe_2O_4$/KFS800 composite, which could be attributed to the C−H and C = C vibrations, implying that the bagasse was carbonized to graphite-like powder during the heating process.

The nitrogen adsorption−desorption isotherms and pore size distributions of $MnFe_2O_4$/KFS800 are shown in Figure 2d. The adsorption−desorption isotherms of $MnFe_2O_4$/KFS800 had a sharp hysteresis loop in the P/P_0 range of 0.4−1.0, and identified as type IV isotherm based on the International Union of Pure and Applied Chemistry classification, which represents a characteristic of mesoporous structures. In addition, the corresponding Barrett−Joyner−Halenda (BJH) pore size distribution shows that the pore size of $MnFe_2O_4$/KFS800 is mainly distributed in the range of 1.5−20 nm and the average pore diameter is 8.5 nm. The specific surface area of magnetic $MnFe_2O_4$/KFS800 is 93 m^2/g, which is larger than that of pure $MnFe_2O_4$ (75 m^2/g), but the total pore volume of $MnFe_2O_4$/KFS800 increased very little (Table 1). In summary,

Table 1. Physical Parameters of Magnetic $MnFe_2O_4$ and $MnFe_2O_4$/KFS800

catalyst	BET surface area (m^2/g)	average pore diameter (nm)	total pore volume (m^3/g)
$MnFe_2O_4$	75	11.9	0.221
$MnFe_2O_4$/KFS800	93	8.5	0.225

after modification, the pore size and total pore volume increased or decreased to a certain extent, but the specific surface area of $MnFe_2O_4$/KFS800 increased by more than 24%, which is beneficial for the adsorption of target pollutants on the surface of the catalyst.

3.2. Degradation of RhB by the $MnFe_2O_4$/KFS800/PDS System. As shown in Figure 3, the degradation efficiency of RhB by PDS alone and $MnFe_2O_4$/KFS800 was 12.5% and 22.1% after 60 min reaction, which indicated that PDS and $MnFe_2O_4$/KFS800 exhibited a limited ability to degradation of RhB. In contrast, RhB degradation efficiency was dramatically enhanced by the addition of $MnFe_2O_4$ into the PDS solution, and 73.6% degradation of RhB can be achieved within 60 min, suggesting that the oxidation ability of PDS was efficiently activated by $MnFe_2O_4$. While, the pure $MnFe_2O_4$ is easy to agglomerate, resulting in not being efficient enough to degrade RhB. The degradation rate of RhB increased to 91.1% with the combination effects of $MnFe_2O_4$/KFS800 and PDS, and the reaction constant reached 0.0322 min^{-1}. The possible reasons could be concluded as follows: (1) $MnFe_2O_4$ and KFS800 have a synergistic catalytic effect. (2) The increase in the specific surface area of $MnFe_2O_4$/KFS800 could generate more active sites to activate PDS to derive more free radicals.

3.3. Degradation of RhB at Optimized Reaction Conditions. Figure 4a shows the degradation curves of RhB by the $MnFe_2O_4$/KFS800/PDS system when the initial concentrations of RhB were 5.35, 10.45, 20.64, and 40.52 mg/L, respectively. The reaction rate constant decreased from 0.0369 to 0.0166 min^{-1} with the increase in the initial concentration. The number of generated free radicals plays a crucial factor in the RhB degradation. When the initial RhB concentration is low, the $SO_4^{\bullet-}$ produced is sufficient for oxidation of pollutants. As the initial concentration of RhB increases, more substrates including RhB and its intermediates were adsorbed on the surface of $MnFe_2O_4$/KFS800, resulting in the acceleration of the reaction among PDS, $MnFe_2O_4$/KFS800, and substrates. Dosage of PDS is also a crucial factor for the degradation of RhB. When the initial PDS concentration increased from 1.2 to 2.0 mM (Figure 4b), the degradation rate was increased dramatically, but when the concentration increased to 2.4 mM, the RhB degradation rate and reaction rate constant did not increase significantly, which may be due to the self-consumption of sulfate radicals in the reaction system and the competitive consumption of sulfate radicals by too many persulfate ions. The pH adaptability of this oxidation processes was studied and it was found that the degradation efficiency could be maintained to a high value when the initial pH was ranged from 5.0 to 6.7 (Figure 4c).

The leaching concentration of Fe and Mn ions could be reduced to a low level as the pH increased (Figure 4d), and achieved 0.0.019and 0.011 mg/L, respectively, when the pH was 6.7. The total Fe and Mn ion leaching concentrations of $MnFe_2O_4$/KFS800 were less than many other reports,[39,40] suggesting that $MnFe_2O_4$ was fairly stable as a catalyst for RhB degradation.

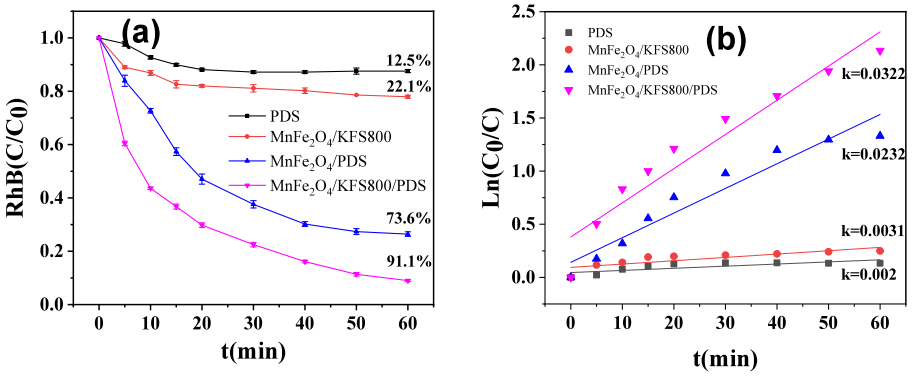

Figure 3. (a) Degradation of RhB by PDS alone, $MnFe_2O_4$/KFS800, $MnFe_2O_4$/PDS, and $MnFe_2O_4$/KFS800/PDS; (b) curve of $\ln(C_0/C)$ vs time. Reaction condition: initial concentration of RhB is 10 mg/L, dosage of catalyst is 0.2 g/L, pH is 6.7, reaction time is 60 min, and reaction temperature is 30 °C.

https://doi.org/10.1021/acsomega.3c06278
ACS Omega 2024, 9, 6455−6465

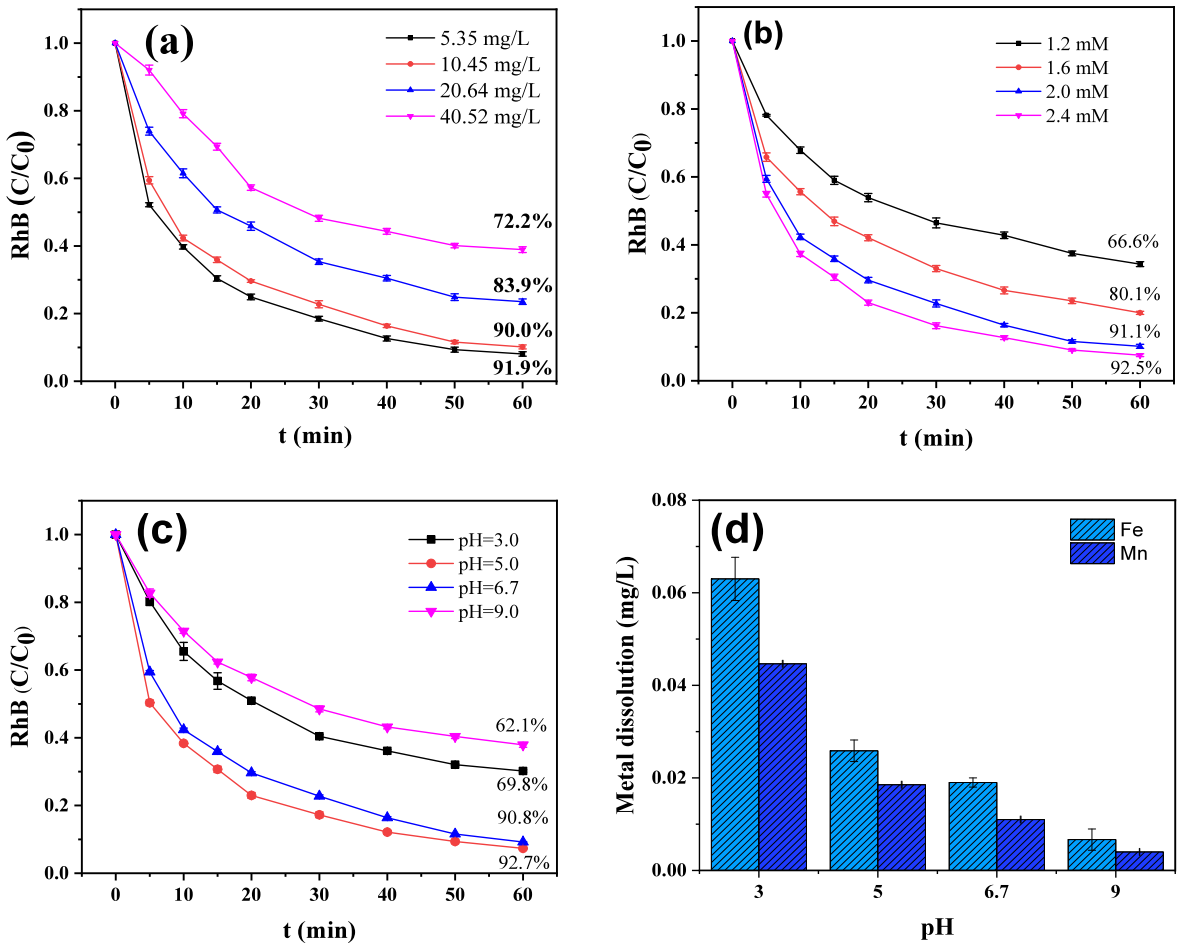

Figure 4. (a) Effect of initial RhB concentration, (b) effect of PDS dosage, and (c) effect of initial pH on RhB degradation in the $MnFe_2O_4$/KFS800/PDS system; (d) metal leaching in the degradation process at different initial pHs.

3.4. Effect of Interference Factor. The influence of several inorganic anions (Cl^-, $H_2PO_4^-$, HCO_3^-, and NO_3^-) and HA on the catalytic performance of the $MnFe_2O_4$/KFS800/PDS system was investigated. As displayed in Figure 5, the degradation efficiency of RhB reached 91.1% after 60 min of reaction without the addition of inorganic anions. When 5 mM inorganic anions (Cl^-, $H_2PO_4^-$, HCO_3^-, and NO_3^-) were added to this degradation system, the degradation of RhB was inhibited to varying degrees, and the degradation efficiency was 77.5%, 73.3%, 81.1%, and 76.3%, respectively. The possible reason for inhibition of Cl^- is that Cl^- has a higher chemical affinity for $SO_4^{\bullet-}$ or •OH, and will generate other oxidizers with weaker oxidation ability (Cl• or $Cl_2^{\bullet-}$).[41] Meanwhile, $H_2PO_4^-$ (HCO_3^- and NO_3^-) could react with $SO_4^{\bullet-}$ or •OH to generate other weaker oxidizing $\bullet H_2PO_4$ ($\bullet HCO_3$ and $\bullet NO_3$).[42,43] In general, inorganic anions have different degrees of RhB degradation in the $MnFe_2O_4$/KFS800/PDS system, and effects of $H_2PO_4^-$ were higher than Cl^-, HCO_3^-, and NO_3^-. In addition, the degradation rate of RhB decreased by only 2.5% when 5 mg/L HA was added to this oxidizing system, which indicates that the presence of HA has basically no effect on the degradation of RhB in the $MnFe_2O_4$/KFS800/PDS system, and this system has good resistance to the water body where HA exists.

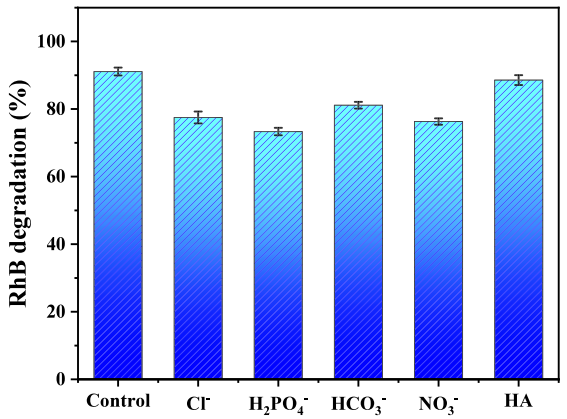

Figure 5. Effects of interference factor on RhB degradation in the $MnFe_2O_4$/KFS800/PDS system.

3.5. Identification of Reactive Radicals. Free radical quenching experiments and EPR analysis were carried out to identify the main reactive species involved in RhB degradation by the $MnFe_2O_4$/KFS800/PDS system. EtOH and TBA were used as radical scavengers for $SO_4^{\bullet-}$ and •OH[44] and were added into this system at the beginning of the reaction. As displayed in Figure 6a, the degradation efficiency of RhB decreased from 91.1% to 68.4% and 77% within 60 min when 1 M TBA and EtOH were added to the $MnFe_2O_4$/KFS800/PDS system, respectively. This shows that the $SO_4^{\bullet-}$ and •OH radicals are produced during the reaction. Moreover, the BQ and L-his were used as quenchers for detecting $O_2^{\bullet-}$ and $^1O_2$,

https://doi.org/10.1021/acsomega.3c06278
ACS Omega 2024, 9, 6455−6465

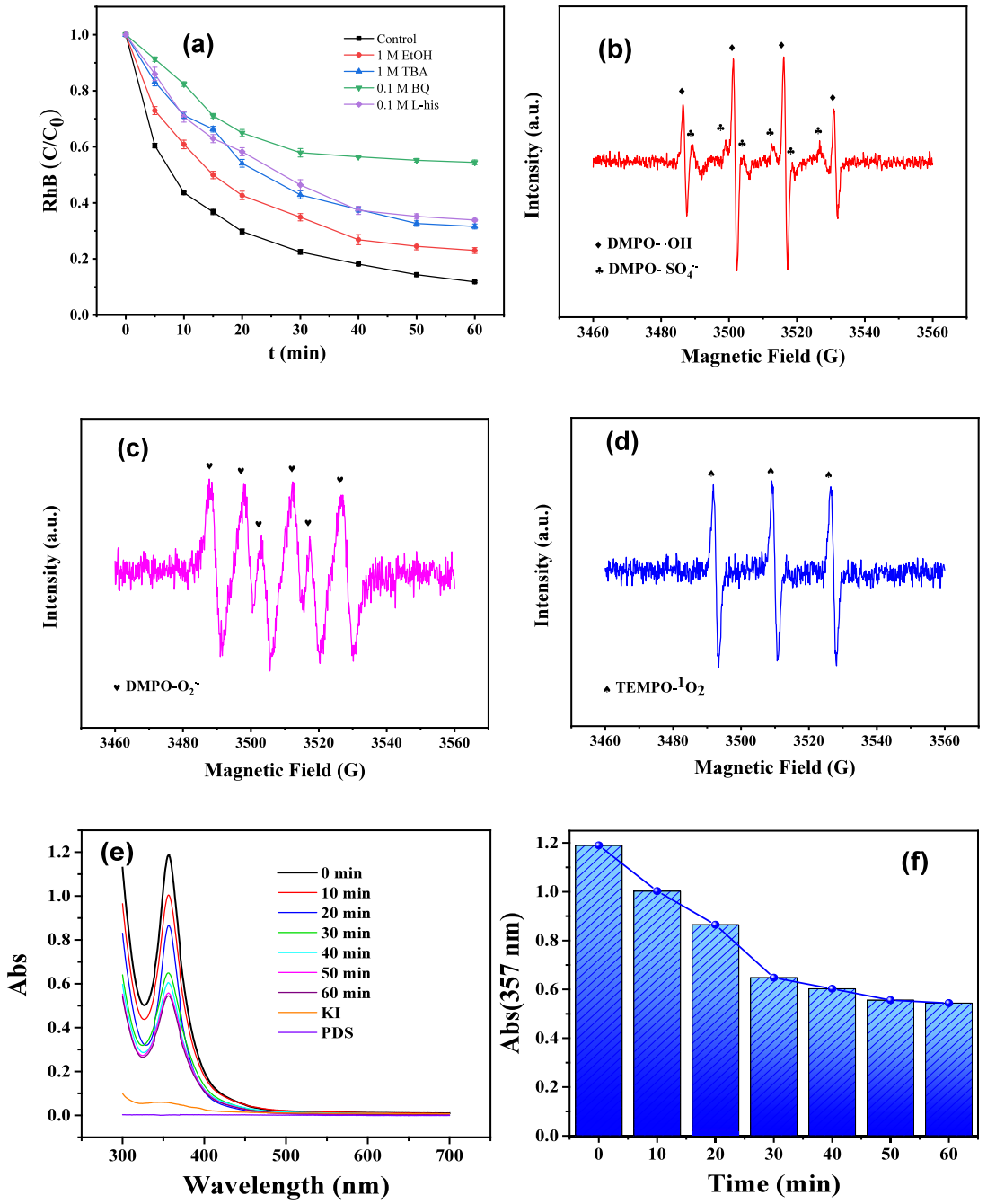

Figure 6. (a) Free radical quenching tests in the catalytic reaction by the $MnFe_2O_4$/KFS800/PDS system; (b)−(d) EPR tests of •OH, $SO_4^{\bullet-}$, $O_2^{\bullet-}$, and $^1O_2$; (e) detection of the residual PDS by iodometric spectrophotometry method; (f) consumption of PDS during the catalytic reaction (determined at λ = 357 nm).

respectively.[45] When 0.1 M BQ and L-his were added into this oxidation system, the degradation rate of RhB decreased by 42.6% and 22.1%, respectively, which proves that $O_2^{\bullet-}$ and $^1O_2$ also contribute to the degradation of RhB. Figure 6b shows the EPR spectroscopy study of this reaction, where it can be seen that $SO_4^{\bullet-}$ and •OH were produced in the catalytic degradation process, and the signal intensity of DMPO−$SO_4^{\bullet-}$ is much higher than that ofDMPO-•OH, which indicates that the main reactive radical in the catalytic degradation process is $SO_4^{\bullet-}$. The quartet characteristic EPR signals of DMPO-$O_2^{\bullet-}$ could be seen in Figure 6c, indicating that $O_2^{\bullet-}$ also played a role in the degradation of RhB. A representative triplet EPR spectrum of TEMPO−$^1O_2$ can be seen in Figure 6d, implying the continuous generation of $^1O_2$ during the reaction. These results were consistent with the free radical quenching results, which supported the existence of both free radical and nonfree radical pathways for pollutant degradation in the $MnFe_2O_4$/KFS800/PDS system. The consumption of the $MnFe_2O_4$/KFS800/PDS system was estimated by iodometric spectrophotometry. As demonstrated in Figure 6e,f, the decreased intensity of absorbance of I_3^- indicated that the concentration of residual PDS is consumed during the reaction, and nearly half of initial PDS was retained in the reaction mixture, which proved that the nonfree radical pathways play an indispensable role in the degradation of RhB.[46]

https://doi.org/10.1021/acsomega.3c06278
ACS Omega 2024, 9, 6455−6465

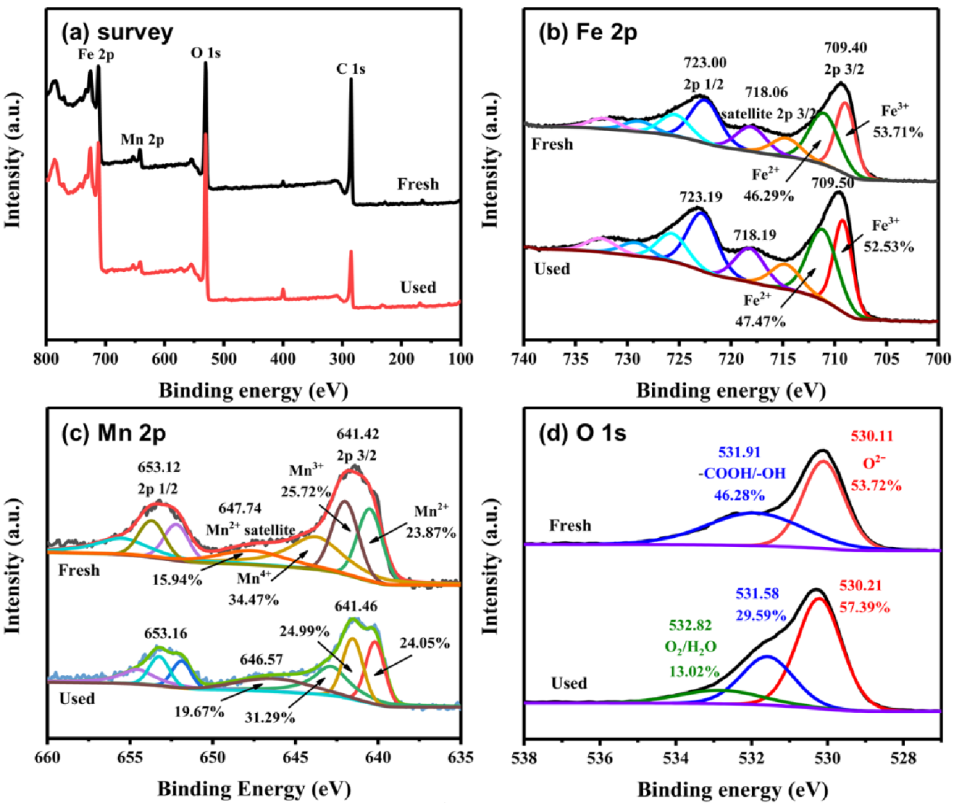

Figure 7. XPS spectrum of (a) survey, (b) Fe 2p, (c) Mn 2p, and (d) O 1s of $MnFe_2O_4$/KFS800 before and after the reaction.

Scheme 1. Proposed Degradation Mechanism in the $MnFe_2O_4$/KFS800/PDS System

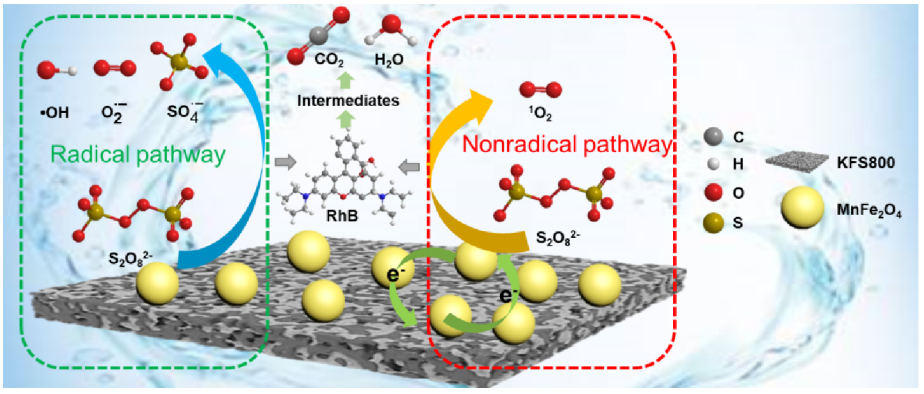

3.6. Proposed Activation Mechanism. To investigate the activation mechanism of PDS by $MnFe_2O_4$/KFS800, the element information on the fresh and used $MnFe_2O_4$/KFS800 were characterized by XPS technology. According to the full survey (Figure 7a), the main elements that existed in the fresh and used $MnFe_2O_4$/KFS80 are Mn, Fe, C, and O. The peak occurring at the binding energy of 709.40 eV (Figure 7b) in the fresh $MnFe_2O_4$/KFS800 is assigned to Fe (2p3/2). The values of Fe (2p3/2) slightly transferred to a higher binding energy value at 709.50 eV after the catalytic reaction, suggesting that the fractions of Fe(II) and Fe(III) in $MnFe_2O_4$/KFS800 changed. Before the reaction, Fe(II) and Fe(III) accounted for 53.71% and 46.29% in the fresh $MnFe_2O_4$/KFS800, but Fe(II) and Fe(III) accounted for 52.53% and 47.47%, respectively, in the used $MnFe_2O_4$/KFS800. This change indicated that electron transfer occurred for a part of Fe(II) in the catalyst during the reaction, and the Fe element on the surface of the catalyst could participate in the catalytic reaction. Figure 7c shows the change in the valence of Mn on the surface of the catalyst before and after the reaction. Before the catalytic reaction, Mn(II), Mn(III), and Mn(IV) accounted for 23.87%, 25.72%, and 34.47% on the catalyst surface, respectively. After the catalytic reaction, Mn(II), Mn(III), and Mn(IV) accounted for 24.05%, 24.99%, and 31.29% on the catalyst surface, respectively. These results indicated that reduction reactions of Fe(III)/Fe(II) and Mn(II)/Mn(III)/Mn(IV) were involved in the activation process.

Generally speaking, the lattice oxygen (O^{2-}) and adsorbed oxygen (−OH/−COOH) on the catalyst surface are crucial factors in the catalytic reaction.[47,48] As illustrated in Figure 7d, before the reaction, the characteristic peak at 530.11 eV corresponds to lattice oxygen (O^{2-}), while the characteristic peak at 531.91 eV belongs to −OH or −COOH anchored on

https://doi.org/10.1021/acsomega.3c06278
ACS Omega 2024, 9, 6455−6465

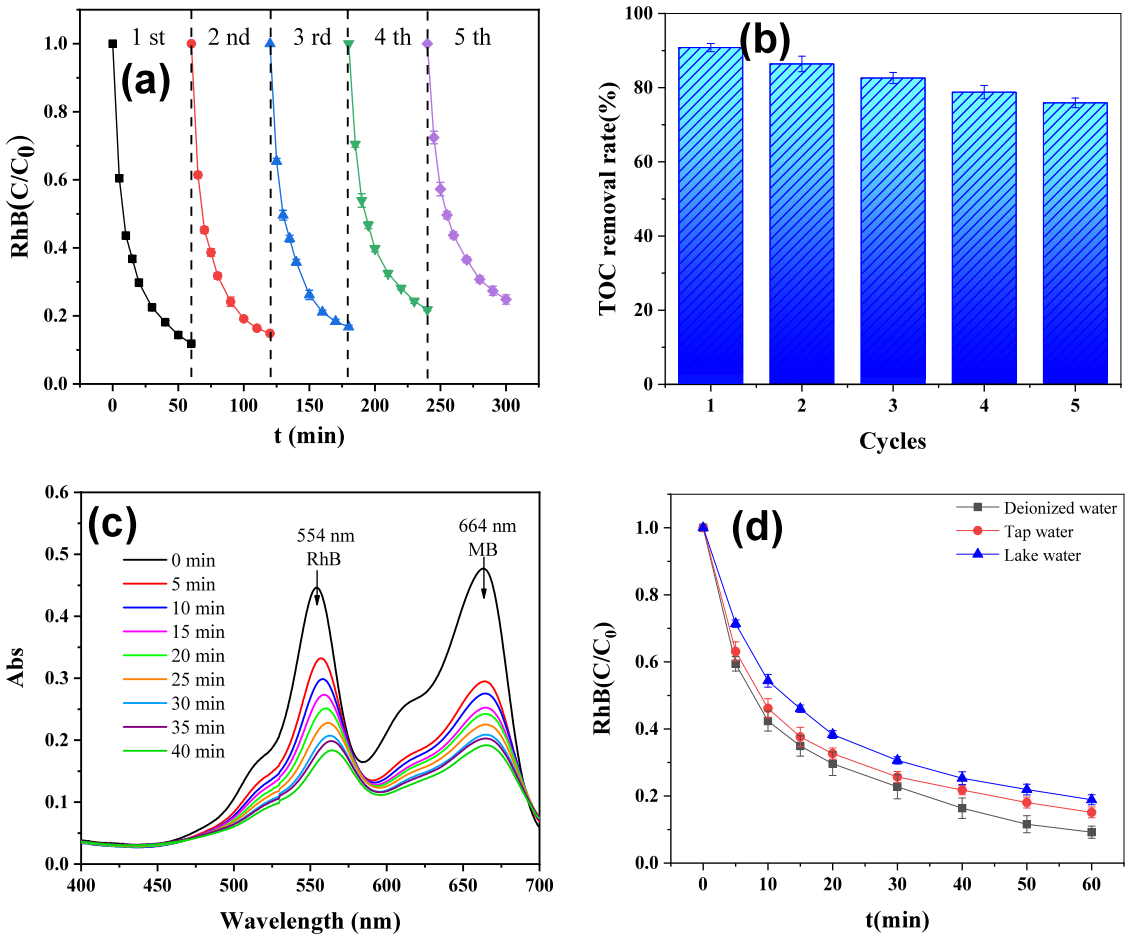

Figure 8. (a) The recyclability of magnetic $MnFe_2O_4$/KFS800 catalyst; (b) TOC removal rate in each cycle test; (c) degradation of the mix dyes by the $MnFe_2O_4$/KFS800/PDS system; (d) degradation of RhB by the $MnFe_2O_4$/KFS800/PDS system in different simulated wastewaters.

the catalyst surface. After the reaction, the characteristic peaks of −OH/−COOH and O^{2-} shifted slightly, the relative content of −OH/−COOH dropped to 29.59%, and the relative content of O^{2-} rose slightly from 53.72% to 57.39%. More importantly, a new characteristic peak at 532.82 eV appeared after the catalytic reaction, indicating migration of H_2O or O_2 to the surface of the catalyst during the catalytic reaction.

Based on the above characterizations and the free radical identification, the possible mechanism of the degradation of RhB by the $MnFe_2O_4$/KFS800/PDS system (Scheme 1) could be described as below.

Oxidation species ($SO_4^{\bullet-}$) could be produced from the activation of PDS by Mn(II) on the surface of $MnFe_2O_4$/KFS80 (eq 2), and Mn(II) was transformed partially into Mn(III). The generated Mn(III) might react with Fe(III) and convert it to Fe(II), while Mn(III) was transformed to Mn(IV) (eq 3). Meanwhile, Fe(II) also reacted with PDS to generate $SO_4^{\bullet-}$ (eq 4).[49] The formed Mn(III), Mn(IV), and Fe(III) reverted back to their pristine chemical state partially via reaction with each other or $SO_4^{\bullet-}$. Oxygen-containing functional groups on the surface of the $MnFe_2O_4$/KFS800 composite could also activate PDS to produce $SO_4^{\bullet-}$ (eq 6 and 7). In addition, under alkaline conditions, •OH could be produced by $SO_4^{\bullet-}$ reaction with H_2O/OH^- (eq 8 and 9), and $O_2^{\bullet-}$ could be produced by $S_2O_8^{2-}$ reaction with H_2O (eq 10 and 11). Under acidic conditions, $O_2^{\bullet-}$ can react with H^+ to produce $^1O_2$ (eq 12). Besides, under alkaline conditions, $O_2^{\bullet-}$ can react with •OH to produce $^1O_2$ (eq 13). Therefore, the oxidative degradation of RhB by the $MnFe_2O_4$/KFS800/PDS system is completed under the combined action of free radicals ($SO_4^{\bullet-}$, •OH, and $O_2^{\bullet-}$) and nonradical ($^1O_2$) (eq 14).

$$Mn^{2+} + S_2O_8^{2-} \rightarrow Mn^{3+} + 2SO_4^{\bullet-} + OH^- \quad (2)$$

$$Fe^{3+} + Mn^{3+} \rightarrow Fe^{2+} + Mn^{4+} \quad (3)$$

$$Fe^{2+} + S_2O_8^{2-} \rightarrow Fe^{3+} + 2SO_4^{\bullet-} + OH^- \quad (4)$$

$$Fe^{2+} + Mn^{3+-} \rightarrow Fe^{3+} + Mn^{2+} \quad (5)$$

$$MnFe_2O_4\ /KFS800\ surface\text{-}OH + S_2O_8^{2-} \rightarrow HSO_4^- + SO_4^{\bullet-} + MnFe_2O_4/KFS800\ surface - O\bullet \quad (6)$$

$$MnFe_2O_4\ /KFS800\ surface - COOH + S_2O_8^{2-} \rightarrow HSO_4^- + SO_4^{\bullet-} + MnFe_2O_4/KFS800\ surface\text{-}COO\bullet \quad (7)$$

$$SO_4^{\bullet-} + H_2O \rightarrow HSO_4^- + \bullet OH \quad (8)$$

$$SO_4^{\bullet-} + OH^- \rightarrow SO_4^{2-} + \bullet OH \quad (9)$$

$$S_2O_8^{2-} + H_2O \rightarrow HO_2^- + 2SO_4^{2-} + 3H^+ \quad (10)$$

https://doi.org/10.1021/acsomega.3c06278
ACS Omega 2024, 9, 6455−6465

$$S_2O_8^{2-} + HO_2^- \rightarrow SO_4^{\bullet-} + SO_4^{2-} + O_2^{\bullet-} + H^+ \quad (11)$$

$$2O_2^{\bullet-} + 2H^+ \rightarrow {}^1O_2 + H_2O_2 \quad (12)$$

$$O_2^{\bullet\bullet-} + \bullet OH \rightarrow {}^1O_2 + OH^- \quad (13)$$

$$SO_4^{\bullet-} + \bullet OH + O_2^{\bullet-} + {}^1O_2 + RhB \rightarrow \text{intermediates} \rightarrow CO_2 + H_2O + \cdots \quad (14)$$

3.7. Reusability and Stability of Magnetic $MnFe_2O_4$/KFS800. It is very important to take the reusability and stability of the catalyst into consideration for large-scale applications. The catalytic performance of recycled $MnFe_2O_4$/KFS800 was tested under the same reaction conditions. The used catalyst was magnetically separated and cleaned by deionized water and ethanol, then redispersed into fresh RhB solution without the addition of fresh catalyst. As seen from Figure 8a,b, the degradation efficiency of RhB and TOC removal rates maintained a high level in the fifth cycles. The slightly loss of catalytic activity can be ascribed to the inevitable loss of catalyst during the recovery process and the residual organic compounds adsorbed on the catalyst. The catalytic performance of the as-synthesized catalyst showed similar degradability in the degradation of an aqueous solution that contains RhB and methylene blue (Figure 8c). Figure 8d exhibited that $MnFe_2O_4$/KFS800/PDS could display satisfactory degradation efficiencies in different simulated wastewaters containing RhB formulated by tap water and lake water, demonstrating its outstanding practical application prospects.

4. CONCLUSIONS

In this work, a magnetic graphite-like porous biochar $MnFe_2O_4$/KFS800 catalyst was prepared by two-step hydrothermal method, and used for the activation of PDS toward the degradation of RhB. The degradation rate of RhB reached 91.1% under optimized initial pH, PDS concentration, and $MnFe_2O_4$/KFS800 dosage. The RhB degradation efficiency decreased with the presence of some inorganic anions in the reaction system, such as Cl^-, $H_2PO_4^-$, HCO_3^-, NO_3^-, but it showed a good resistance to the water body where HA existed. Moreover, through quenching test, EPR research, and XPS analysis results, the proposed mechanism of the $MnFe_2O_4$/KFS800/PDS system shows a synergic effect of free radicals ($SO_4^{\bullet-}$, $\bullet OH$, and $O_2^{\bullet-}$) and nonfree radicals ($^1O_2$). This study might provide a new method to prepare recoverable catalysts to activate PDS for the degradation of organic pollutants by decorating graphite-like porous carbon material with $MnFe_2O_4$.

AUTHOR INFORMATION

Corresponding Authors

Xinde Jiang − *School of Civil Engineering and Architecture, Nanchang Institute of Technology, Nanchang 330099, China*; orcid.org/0000-0003-3758-3863; Email: jxd@nit.edu.cn

Zhanmeng Liu − *School of Civil Engineering and Architecture, Nanchang Institute of Technology, Nanchang 330099, China*; orcid.org/0000-0002-1652-6774; Phone: (+86) 791 82096402; Email: ustblzm@sina.com

Authors

Zhuoru Tan − *School of Civil Engineering and Architecture, Nanchang Institute of Technology, Nanchang 330099, China*

Guixian Jiang − *School of Civil Engineering and Architecture, Nanchang Institute of Technology, Nanchang 330099, China*

Chang Liu − *School of Civil Engineering and Architecture, Nanchang Institute of Technology, Nanchang 330099, China*

Guiqing Gao − *School of Civil Engineering and Architecture, Nanchang Institute of Technology, Nanchang 330099, China*

Complete contact information is available at: https://pubs.acs.org/10.1021/acsomega.3c06278

Funding

This work was financially supported by National Natural Science Foundation of China (52260005, 21706113), Natural Science Foundation of Jiangxi (20212BAB204041, 20232BAB215011), Key Research and Development Program of Jiangxi Province (20203BBGL73230), and Natural Science Foundation of Jiangxi Provincial Department of Education (GJJ201921, GJJ211905).

Notes

The authors declare no competing financial interest.

ACKNOWLEDGMENTS

The manuscript was written through contributions of all authors. All authors have given approval to the final version of the manuscript.

REFERENCES

(1) Ning, X.-A.; Wang, J.-Y.; Li, R.-J.; Wen, W.-B.; Chen, C.-M.; Wang, Y.-J.; Yang, Z.-Y.; Liu, J.-Y. Fate of volatile aromatic hydrocarbons in the wastewater from six textile dyeing wastewater treatment plants. *Chemosphere* **2015**, *136*, 50−55.

(2) Hussein, F. H. Chemical properties of treated textile dyeing wastewater. *Asian J. Chem.* **2013**, *25* (16), 9393−9400.

(3) Ismail, G. A.; Sakai, H. Review on effect of different type of dyes on advanced oxidation processes (AOPs) for textile color removal. *Chemosphere* **2022**, *291*, 132906.

(4) Dalvand, A.; Gholami, M.; Joneidi, A.; Mahmoodi, N. M. Dye removal, energy consumption and operating cost of electrocoagulation of textile wastewater as a clean process. *Clean: Soil, Air, Water* **2011**, *39* (7), 665−672.

(5) Nidheesh, P. V.; Divyapriya, G.; Ezzahra Titchou, F.; Hamdani, M. Treatment of textile wastewater by sulfate radical based advanced oxidation processes. *Sep. Purif. Technol.* **2022**, *293*, 121115.

(6) Giannakis, S.; Lin, K.-Y. A.; Ghanbari, F. A review of the recent advances on the treatment of industrial wastewaters by Sulfate Radical-based Advanced Oxidation Processes (SR-AOPs). *Chem. Eng. J.* **2021**, *406*, 127083.

(7) Ushani, U.; Lu, X.; Wang, J.; Zhang, Z.; Dai, J.; Tan, Y.; Wang, S.; Li, W.; Niu, C.; Cai, T.; Wang, N.; Zhen, G. Sulfate radicals-based advanced oxidation technology in various environmental remediation: A state-of-the−art review. *Chem. Eng. J.* **2020**, *402*, 126232.

(8) Tan, J.; Chen, X.; Shang, M.; Cui, J.; Li, D.; Yang, F.; Zhang, Z.; Zhang, H.; Wu, Q.; Li, Y.; Lin, X. N-doped biochar mediated peroxydisulfate activation for selective degradation of bisphenol A: The key role of potential difference-driven electron transfer mechanism. *Chem. Eng. J.* **2023**, *468*, 143476.

(9) Sonawane, S.; Rayaroth, M. P.; Landge, V. K.; Fedorov, K.; Boczkaj, G. Thermally activated persulfate-based advanced oxidation processes-recent progress and challenges in mineralization of

persistent organic chemicals: A review. *Curr. Opin. Chem. Eng.* **2022**, *37*, 100839.
(10) Hu, L.; Zhang, G.; Wang, Q.; Wang, X.; Wang, P. Effect of microwave heating on persulfate activation for rapid degradation and mineralization of p-nitrophenol. *ACS Sustain. Chem. Eng.* **2019**, *7* (13), 11662.
(11) Achola, L. A.; Ghebrehiwet, A.; Macharia, J.; Kerns, P.; He, J.; Fee, J.; Tinson, C.; Shi, J.; March, S.; Jain, M.; Suib, S. L. Enhanced visible-light-assisted peroxymonosulfate activation on cobalt-doped mesoporous iron oxide for orange II degradation. *Appl. Catal. B* **2020**, *263*, 118332.
(12) Zhang, T.; Yang, Y.; Li, X.; Yu, H.; Wang, N.; Li, H.; Du, P.; Jiang, Y.; Fan, X.; Zhou, Z. Degradation of sulfamethazine by persulfate activated with nanosized zero-valent copper in combination with ultrasonic irradiation. *Sep. Purif. Technol.* **2020**, *239*, 116537.
(13) Shao, P.; Yu, S.; Duan, X.; Yang, L.; Shi, H.; Ding, L.; Tian, J.; Yang, L.; Luo, X.; Wang, S. Potential difference driving electron transfer via defective carbon nanotubes toward selective oxidation of organic micropollutants. *Environ. Sci. Technol.* **2020**, *54* (13), 8464−8472.
(14) Anipsitakis, G. P.; Dionysiou, D. D. Radical generation by the interaction of transition metals with common oxidants. *Environ. Sci. Technol.* **2004**, *38*, 3705.
(15) Wang, Z.; Su, J.; Huang, T.; Liu, Y.; Zhao, T.; Li, J.; Zhang, L. Biocrystal-encased manganese ferrite coupling with peroxydisulfate: Synergistic mechanism of adsorption and catalysis towards tetracycline removal. *Chem. Eng. J.* **2023**, *468*, 143580.
(16) Tan, J.; Wang, J.; Tan, Z.; Yu, M.; Yang, Z.; Ren, Z.; Li, Y.; Zhang, Y.; Lin, X. Efficient activation of peroxydisulfate by a novel magnetic nanocomposite lignin hydrogel for contaminant degradation: Radical and nonradical pathways. *Chem. Eng. J.* **2023**, *451*, 138504.
(17) Wang, M.; Cui, Y.; Cao, H.; Wei, P.; Chen, C.; Li, X.; Xu, J.; Sheng, G. Activating peroxydisulfate with Co_3O_4/$NiCo_2O_4$ double-shelled nanocages to selectively degrade bisphenol A-A nonradical oxidation process. *Appl. Catal. B* **2021**, *282*, 119585.
(18) Cai, C.; Zhang, Z.; Liu, J.; Shan, N.; Zhang, H.; Dionysiou, D. D. Visible light-assisted heterogeneous Fenton with $ZnFe_2O_4$ for the degradation of Orange II in water. *Appl. Catal. B* **2016**, *182*, 456−468.
(19) Ding, Y.; Wang, X.; Fu, L.; Peng, X.; Pan, C.; Mao, Q.; Wang, C.; Yan, J. Nonradicals induced degradation of organic pollutants by peroxydisulfate (PDS) and peroxymonosulfate (PMS): Recent advances and perspective. *Sci. Total Environ.* **2021**, *765*, 142794.
(20) Fu, H.; Ma, S.; Zhao, P.; Xu, S.; Zhan, S. Activation of peroxymonosulfate by graphitized hierarchical porous biochar and $MnFe_2O_4$ magnetic nanoarchitecture for organic pollutants degradation: *Structure dependence and mechanism*. *Chem. Eng. J.* **2019**, *360*, 157−170.
(21) Zhou, X.; Kong, L.; Jing, Z.; Wang, S.; Lai, Y.; Xie, M.; Ma, L.; Feng, Z.; Zhan, J. Facile synthesis of superparamagnetic beta-CD-$MnFe_2O_4$ as a peroxymonosulfate activator for efficient removal of 2,4- dichlorophenol: structure, performance, and mechanism. *J. Hazard. Mater.* **2020**, *394*, 122528.
(22) Gao, Z.; Zhu, J.; Zhu, Q.; Wang, C.; Cao, Y. Spinel ferrites materials for sulfate radical-based advanced oxidation process: A review. *Sci. Total Environ.* **2022**, *847*, 157405.
(23) Chen, G.; Zhang, X.; Gao, Y.; Zhu, G.; Cheng, Q.; Cheng, X. Novel magnetic MnO_2/$MnFe_2O_4$ nanocomposite as a heterogeneous catalyst for activation of peroxymonosulfate (PMS) toward oxidation of organic pollutants. *Sep. Purif. Technol.* **2019**, *213*, 456−464.
(24) Meng, X.; He, Q.; Song, T.; Ge, M.; He, Z.; Guo, C. Activation of peroxydisulfate by magnetically separable rGO/$MnFe_2O_4$ toward oxidation of tetracycline: Efficiency, mechanism and degradation pathways. *Sep. Purif. Technol.* **2022**, *282*, 120137.
(25) Ma, D.; Yang, Y.; Liu, B.; Xie, G.; Chen, C.; Ren, N.; Xing, D. Zero-valent iron and biochar composite with high specific surface area via K_2FeO_4 fabrication enhances sulfadiazine removal by persulfate activation. *Chem. Eng. J.* **2021**, *408*, 127992.
(26) Nie, C.; Ao, Z.; Duan, X.; Wang, C.; Wang, S.; An, T. Degradation of aniline by electrochemical activation of peroxydisulfate at MWCNT cathode: The proofed concept of nonradical oxidation process. *Chemosphere* **2018**, *206*, 432.
(27) Ren, W.; Xiong, L.; Yuan, X.; Yu, Z.; Zhang, H.; Duan, X.; Wang, S. Activation of peroxydisulfate on carbon nanotubes: Electron-transfer mechanism. *Environ. Sci. Technol.* **2019**, *53*, 14595.
(28) Manz, K. E.; Kulaots, I.; Greenley, C. A.; Landry, P. J.; Lakshmi, K. V.; Woodcock, M. J.; Hellerich, L.; Bryant, J. D.; Apfelbaum, M.; Pennell, K. D. Low-temperature persulfate activation by powdered activated carbon for simultaneous destruction of perfluorinated carboxylic acids and 1,4-dioxane. *J. Hazard. Mater.* **2023**, *442*, 129966.
(29) Zhang, Y.; Zhang, B. T.; Teng, Y.; Zhao, J.; Sun, X. Heterogeneous activation of persulfate by carbon nanofiber supported Fe_3O_4@carbon composites for efficient ibuprofen degradation. *J. Hazard. Mater.* **2021**, *401*, 123428.
(30) Qin, H.; Cheng, H.; Li, H.; Wang, Y. Degradation of ofloxacin, amoxicillin and tetracycline antibiotics using magnetic core−shell $MnFe_2O_4$@C-NH_2 as a heterogeneous Fenton catalyst. *Chem. Eng. J.* **2020**, *396*, 125304.
(31) Meng, X.; Song, T.; Zhang, C.; Wang, H.; Ge, M.; Guo, C. Magnetic $MnFe_2O_4$ nanoparticles anchored on sludge-derived biochar in activating peroxydisulfate for levofloxacin degradation: Mechanism, degradation pathways and cost analysis. *J. Environ. Chem. Eng.* **2023**, *11* (3), 110241.
(32) Li, S.; Liu, X.; Zheng, Y.; Ma, J.; You, S.; Zheng, H. Effective peroxydisulfate activation by CQDs-$MnFe_2O_4$@ZIF-8 catalyst for complementary degradation of bisphenol A by free radicals and non-radical pathways. *Chin. Chem. Lett.* **2023**, 108971. .
(33) Chen, X.; Li, H.; Lai, L.; Zhang, Y.; Chen, Y.; Li, X.; Liu, B.; Wang, H. Peroxymonosulfate activation using $MnFe_2O_4$ modified biochar for organic pollutants degradation: Performance and mechanisms. *Sep. Purif. Technol.* **2023**, *308*, 122886.
(34) Zhao, Y.; Cao, Z.; Chen, Y.; Jia, Y.; Wang, Q.; Cheng, H. Heterostructure coal-bearing strata kaolinite/$MnFe_2O_4$ composite for activation of peroxydisulfate to efficiently degrade chlortetracycline hydrochloride. *Colloid. Surface A* **2022**, *643*, 128789.
(35) Dai, L.; J, X.; Lin, J.; L, W.; Cai, H.; Zou, J.; Ma, J. Iodometric spectrophotometric determination of peroxydisulfate in hydroxylamine-involved AOPs: 15min or 15 s for oxidative coloration? *Chemosphere* **2021**, *272*, 128577.
(36) Guan, R.; Yuan, X.; Wu, Z.; Wang, H.; Jiang, L.; Zhang, J.; Li, Y.; Zeng, G.; Mo, D. Accelerated tetracycline degradation by persulfate activated with heterogeneous magnetic $Ni_xFe_{3-x}O_4$ catalysts. *Chem. Eng. J.* **2018**, *350*, 573−584.
(37) Dhanalaxmi, K.; Yadav, R.; Kundu, S. K.; Reddy, B. M.; Amoli, V.; Sinha, A. K.; Mondal, J. $MnFe_2O_4$ nanocrystals wrapped in a porous organic polymer: A designed architecture for water-splitting photocatalysis. *Chem.-Eur. J.* **2016**, *22* (44), 15639−15644.
(38) Xu, L. S.; Sun, X. B.; Hong, J.-M.; Zhang, Q. Peroxymonosulfate activation by α-MnO_2/$MnFe_2O_4$ for norfloxacin degradation: *Efficiency and mechanism*. *J. Phys. Chem. Solids* **2021**, *153*, 110029.
(39) Yao, Y.; Hu, H.; Zheng, H.; Hu, H.; Tang, Y.; Liu, X.; Wang, S. Nonprecious bimetallic Fe, Mo-embedded N-enriched porous biochar for efficient oxidation of aqueous organic contaminants. *J. Hazard. Mater.* **2022**, *422*, 126776.
(40) Li, L.; Zhang, Q.; She, Y.; Yu, Y.; Hong, J. High-efficiency degradation of bisphenol A by heterogeneous Mn−Fe layered double oxides through peroxymonosulfate activation: Performance and synergetic mechanism. *Sep. Purif. Technol.* **2021**, *270*, 118770.
(41) Hu, L.; Zhang, G.; Liu, M.; Wang, Q.; Wang, P. Enhanced degradation of Bisphenol A (BPA) by peroxymonosulfate with Co_3O_4-Bi_2O_3 catalyst activation: Effects of pH, inorganic anions, and water matrix. *Chem. Eng. J.* **2018**, *338*, 300−310.
(42) Neta, P.; Huie, R. E.; Ross, A. B. Rate Constants for Reactions of Inorganic Radicals in Aqueous Solution. *J. Phys. Chem. Ref. Data* **1988**, *17* (3), 1027−1284.
(43) Wang, L.; Lan, X.; Peng, W.; Wang, Z. Uncertainty and misinterpretation over identification, quantification and transforma-

https://doi.org/10.1021/acsomega.3c06278
ACS Omega 2024, 9, 6455−6465

tion of reactive species generated in catalytic oxidation processes: A review. *J. Hazard. Mater.* **2021**, *408*, 124436.
(44) Ren, W.; Gao, J.; Lei, C.; Xie, Y.; Cai, Y.; Ni, Q.; Yao, J. Recyclable metal-organic framework/cellulose aerogels for activating peroxymonosulfate to degrade organic pollutants. *Chem. Eng. J.* **2018**, *349*, 766−774.
(45) Shang, Y.; Chen, C.; Zhang, P.; Yue, Q.; Li, Y.; Gao, B.; Xu, X. Removal of sulfamethoxazole from water via activation of persulfate by Fe_3C@NCNTs including mechanism of radical and nonradical process. *Chem. Eng. J.* **2019**, *375*, 122004.
(46) Li, Y.; Wang, C.; Wang, F.; Liu, W.; Chen, L.; Zhao, C.; Fu, H.; Wang, P.; Duan, X. Nearly zero peroxydisulfate consumption for persistent aqueous organic pollutants degradation via nonradical processes supported by in-situ sulfate radical regeneration in defective MIL-88B(Fe). *Appl. Catal. B* **2023**, *331*, 122699.
(47) Ren, Y.; Lin, L.; Ma, J.; Yang, J.; Feng, J.; Fan, Z. Sulfate radicals induced from peroxymonosulfate by magnetic ferrospinel MFe_2O_4 (M = Co, Cu, Mn, and Zn) as heterogeneous catalysts in the water. *Appl. Catal. B* **2015**, *165*, 572−578.
(48) Yu, X.; Sun, J.; Li, G.; Huang, Y.; Li, Y.; Xia, D.; Jiang, F. Integration of $\cdot SO_4^-$ based AOP mediated by reusable iron particles and a sulfidogenic process to degrade and detoxify Orange II. *Water Res.* **2020**, *174*, 115622.
(49) Yan, J.; Chen, Y.; Qian, L.; Gao, W.; Ouyang, D.; Chen, M. Heterogeneously catalyzed persulfate with a CuMgFe layered double hydroxide for the degradation of ethylbenzene. *J. Hazard. Mater.* **2017**, *338*, 372−380.

https://doi.org/10.1021/acsomega.3c06278
ACS Omega 2024, 9, 6455−6465